



This article appeared in a journal published by Elsevier. The attached copy is furnished to the author for internal non-commercial research and education use, including for instruction at the authors institution and sharing with colleagues.

Other uses, including reproduction and distribution, or selling or licensing copies, or posting to personal, institutional or third party websites are prohibited.

In most cases authors are permitted to post their version of the article (e.g. in Word or Tex form) to their personal website or institutional repository. Authors requiring further information regarding Elsevier's archiving and manuscript policies are encouraged to visit:

<http://www.elsevier.com/copyright>



Contents lists available at ScienceDirect

## Ultramicroscopy

journal homepage: [www.elsevier.com/locate/ultramic](http://www.elsevier.com/locate/ultramic)Structural imaging of  $\beta$ - $\text{Si}_3\text{N}_4$  by spherical aberration-corrected high-resolution transmission electron microscopy

Zaoli Zhang\*, Ute Kaiser\*

Materials Science Electron Microscopy, Ulm University, 89069 Ulm, Germany

## ARTICLE INFO

## Article history:

Received 7 November 2007

Received in revised form

18 March 2009

Accepted 17 April 2009

## Keywords:

Spherical-aberration corrector

High-resolution electron microscopy

Ceramic

 $\text{Si}_3\text{N}_4$ 

## ABSTRACT

Modern transmission electron microscopes (TEM) allow utilizing the spherical aberration coefficient as an additional free parameter for optimizing resolution and contrast. By tuning the spherical aberration coefficient of the objective lens, isolated nitrogen atom columns as well as the Si–N dumbbells within the six-membered ring were imaged in  $\beta$ - $\text{Si}_3\text{N}_4$  along  $[0001]$  and  $[000\bar{1}]$  projections with a dumbbell spacing of 0.94 Å in white atom contrast. This has been obtained with negative or positive spherical aberration coefficient. We clarify contrast details in  $\beta$ - $\text{Si}_3\text{N}_4$  by means of extended image calculations. A simple procedure has been shown for pure phase imaging, which is restricted to linear imaging conditions.

© 2009 Elsevier B.V. All rights reserved.

## 1. Introduction

Silicon nitride ( $\text{Si}_3\text{N}_4$ ) ceramics have been intensively investigated for many years largely because they exhibit unique high temperature mechanical and physical properties. Great efforts were made to understand local compositions, interface structures and local bonding behaviours between dopants (i.e. rare earths) and  $\text{Si}_3\text{N}_4$  grains, and to image the six-membered rings of  $\langle 0001 \rangle$  projection [1,2]. Some interesting results have been reported by STEM and associated EELS analysis techniques [3–5]. However, by STEM imaging, the nitrogen atom columns in the six-membered rings of the  $\text{Si}_3\text{N}_4$   $\langle 0001 \rangle$  projection cannot be well resolved.

In the past decade, the information limit around 1 Å could be fully exploited by focus-series reconstruction [6–8] and the isolated N atom columns between the six-membered rings of  $\text{Si}_3\text{N}_4$  were imaged [9,10]. However, the Si–N dumbbells in the reconstructed images could be hardly discerned. The breakthrough in HRTEM [11] was achieved with the advent of the double-hexapole aberration corrector [12,13]. Imaging with variable spherical aberration proposed theoretically [14,15] is now a practical reality [16]. It was found that negative  $C_s$  imaging conditions, resulting in ‘white-atom’ contrast on dark background, are especially useful for imaging weakly scattering light atoms in the surrounding of strongly scattering heavy atoms, when the linear theory can be applied [11,16,17]. However, the optimum

choice of spherical aberration coefficient and defocus depends on the specimen thickness [18]. Applying negative  $C_s$  imaging conditions, the nitrogen and silicon atoms in the six-membered ring of  $\text{Si}_3\text{N}_4$  could be imaged in white atom contrast in most thin specimen areas [19–21]. It should be noted that it is still not trivial yet to clearly image the hexagonal lattice of  $\text{Si}_3\text{N}_4$  with a Si–N dumbbell spacing of 0.094 nm in  $\langle 0001 \rangle$  direction, simply because this distance approaches the information limit of the present  $C_s$ -corrected microscopes.

In this paper, we present a more extended HRTEM study on the imaging conditions for the six-membered rings along the  $\langle 0001 \rangle$  direction in  $\text{Si}_3\text{N}_4$  using a mid-voltage (300 kV) TEM equipped with an imaging side spherical aberration corrector. By employing comprehensive image calculation and analysis, we reveal structure and contrast characteristics of  $\beta$ - $\text{Si}_3\text{N}_4$ .

## 2. Experimental procedures

The experiments were carried out using a FEI Titan (80–300) with field-emission gun and an objective lens aberration corrector. The coefficient of chromatic aberration for this microscope is 1.5 mm. By resolving Si  $[112]$  dumbbells [22], we proved that the point to point resolution of the microscope is 0.78 Å at 300 kV. In these experiments, all HRTEM images were taken on a  $1024 \times 1024$  pixel CCD camera at a magnification of 1.4, 1.25 M and 620 K, respectively.

$\text{Si}_3\text{N}_4$  polycrystalline ceramics with a composition of  $\text{Si}_3\text{N}_4$ –2MgO–7.2La<sub>2</sub>O<sub>3</sub> (in wt%) were used for atomic imaging, in which the amorphous phase is in total 11.4 wt% of the  $\text{Si}_3\text{N}_4$

\* Corresponding authors.

E-mail addresses: [zhang\\_zaoali@yahoo.com](mailto:zhang_zaoali@yahoo.com) (Z. Zhang), [ute.kaise@uni.ulm.de](mailto:ute.kaise@uni.ulm.de) (U. Kaiser).

**Table 1**Maximum measured values of the axial aberration coefficients for different  $C_s$  values used in the experiments (1), (2) and (3), respectively.

Objective lens aberrations (abbreviations)	(1) $C_s \sim -0.5 \mu\text{m (nm)}$	(2) $C_s \sim +1 \mu\text{m (nm)}$	(3) $C_s \sim +10 \mu\text{m (nm)}$
3-fold astigmatism (A2)	<5	<100	$\sim 50$
Axial coma (B2)	<3	<20	$\sim 50$
Spherical aberration ( $C_s$ )	$\sim -500$	<1000	<10,000
4-fold astigmatism (A3)	<100	<100	<1000
Star aberration (S3)	<100	<1000	$\sim 300$
5-fold astigmatism (A4)	<5000	<130,000	<160,000

ceramic system. A large  $\text{Si}_3\text{N}_4$  grain was chosen for structural imaging after aligning along the  $\langle 0001 \rangle$  zone axis.

The microscope column was preliminarily aligned before the  $C_s$  corrector was started. The alignment of the  $C_s$  corrector was performed using the CEOS software [13] based on the aberration measurements deduced from Zemlin tableaux [23]. After iterative corrections using the amorphous area at the edge of the specimen, we achieved the aberration coefficients as listed in Table 1. In this table we present for the different  $C_s$  values all the other axial aberration coefficients. Only the maximum values are given. Images were taken at the foci ranging from an over-focus of about 15 nm to under-focus of 5 nm. Before tuning, the defocus was reset to zero when minimum contrast at the edge of amorphous carbon was reached, and then the defocus value was calibrated corresponding to the minimum contrast conditions.

We performed image calculations employing the JEMS package based on the Bloch wave method [24]. The input values of the aberration coefficients and their orientations (A2, B2) as well as spherical aberration ( $C_s$ ) used in the calculation were set to the corresponding experimental values in Table 1. Both image and beam shift were set to zero. The semi-angle of the beam convergence was set to 0.2 mrad simply because it gave the best match to the experimental images, and this value also approximately corresponds to the information limit of our microscope as was found from varying the envelope function. The Gaussian focus spread was set to 2.9 nm. These values approximately correspond to the information limit of our microscope. The Debye-Waller factors are set to  $0.005 \text{ nm}^2$  for the Si and the N atoms. Image calculations were made for different values of the coefficient of the spherical aberration.

### 3. Results and discussion

#### 3.1. Crystal structure and image calculation

##### 3.1.1. The structure of $\beta\text{-Si}_3\text{N}_4$

The  $\beta\text{-Si}_3\text{N}_4$  crystal is hexagonal with lattice constants:  $a = b = 0.7604 \text{ nm}$ ,  $c = 0.2906 \text{ nm}$  and a space-group of  $P 6_3/m$  (No.176) [25]. The spacing of the Si–N dumbbell along  $c$ -axis  $\langle 0001 \rangle$  projection in the lattice has been calculated to be  $0.94 \text{ \AA}$ . The crystal structure models along the  $\langle 0001 \rangle$  orientation (Fig. 1) clearly display that within the six-membered rings the Si–N dumbbell orientation is either clockwise, i.e.  $[0001]$ , or counter-clockwise, i.e.  $[000\bar{1}]$ .

##### 3.1.2. Point-resolution requirements and pure phase contrast images

To resolve Si–N dumbbells in  $\langle 0001 \rangle$  projection ( $d_{\min} = 0.094 \text{ nm}$ ) at 300 kV and Scherzer defocus, the required  $C_s$  value is smaller than  $75 \mu\text{m}$ . This small value can only be realized by means of a  $C_s$ -corrected microscope. Fig. 2 shows an image series of  $\text{Si}_3\text{N}_4$  with a thickness of 2.0 nm. The images were calculated in

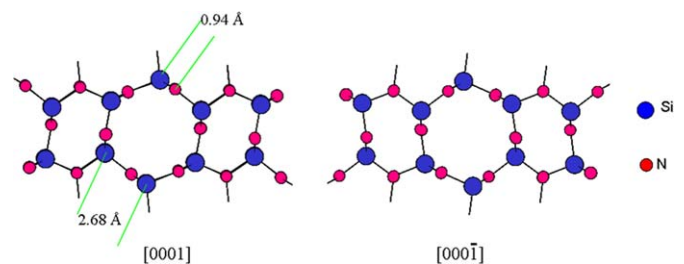


**Fig. 1.** The atomic structure of  $\beta\text{-Si}_3\text{N}_4$  along the  $\langle 0001 \rangle$  projection. Note that the Si and N atom arrangements in the six-membered rings differ, either clockwise,  $[0001]$  or counter-clockwise, i.e.  $[000\bar{1}]$ . In the model of this article, red and blue dots denote nitrogen and silicon, respectively.

$[0001]$  projection for decreasing absolute values of the spherical aberration coefficient near Scherzer defocus. The results demonstrate that the visibility of the Si–N dumbbells dramatically increases at a  $C_s$  value around  $10 \mu\text{m}$  and, in accordance with [17], that a negative  $C_s$  value is most favourable for resolving the Si–N dumbbells and obtaining sharp dumbbell images. The images *a* and *b* are not fully complementary (for instance, compare the most right two images of the lower row). This difference indicates that already at an object thickness of 2.0 nm (there are approximately 7 Si and 7 N atoms along this projection) non-linear interactions (interference between non-diffracted and diffracted beams as well as between diffracted beams) contribute significantly to the image contrast.

Fig. 3 shows the simulated image intensity calculated at complementary  $C_s$  conditions for different object thicknesses. In addition, we calculated the sum and difference of the images depicted in row ( $a+b$ ) and row ( $a-b$ ), respectively. The amplitude and phase contrast transfer functions (CTF) for identical but complementary imaging conditions are plotted on the right of Fig. 3. Only in case *a*, amplitude contrast and phase contrast contribute to the image contrast with the same sign, resulting in stronger contrast and sharper images. For weak phase object (corresponding to 0.5 nm column), the enhanced contrast and the sharper atom column images under negative  $C_s$  and over-focus condition (presented in *a*) over the complementary case (presented in *b*) can be understood from the phase CTFs presented on the right. In the sum image ( $a+b$ ) for the thickness of 0.5 nm, the image intensity is approximately zero. This behaviour does not hold for larger thicknesses, where the non-linear terms contribute appreciably to the image intensity, and amplitude CTF has to be considered [16,26,27]. It should be noted that for thicknesses as large as 10 nm, the positive  $C_s$  image shows white atom columns too, because the amplitude contribution is dominant. Moreover, we can conclude that for the case of  $\beta\text{-Si}_3\text{N}_4$ , dynamic effects have remarkable contribution to the strong ‘white-atom’ contrast observed in *a* at a thickness as small as 2.0 nm. The summation

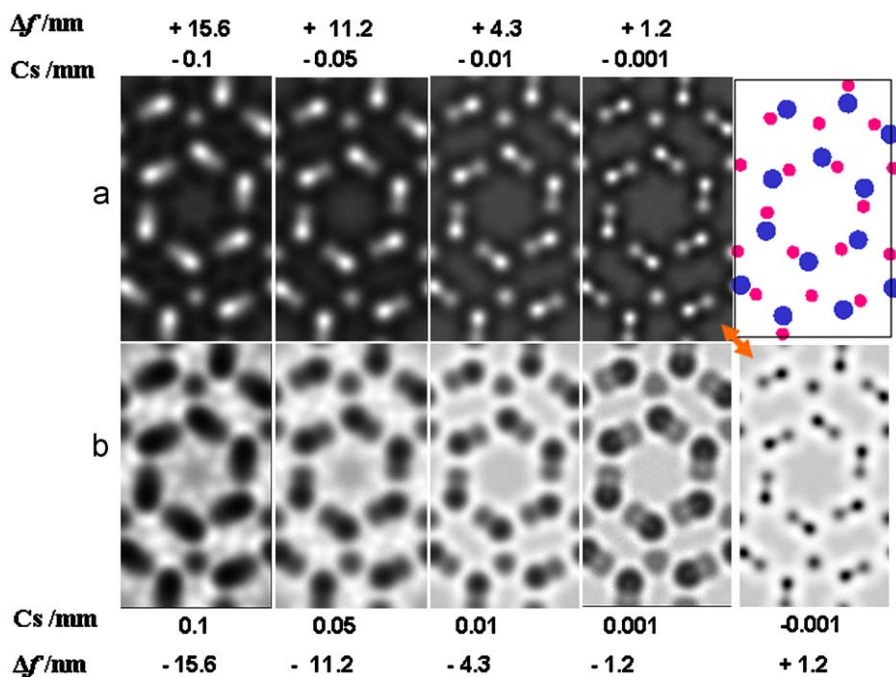


**Fig. 2.** HRTEM image series (thickness 2.0 nm) calculated along  $[0001]$   $\beta$ - $\text{Si}_3\text{N}_4$  for decreasing absolute  $C_s$  and defocus values, indicating the required  $C_s$  value to visualize Si–N dumbbells. For comparison, a mathematically inverted image from  $C_s = -0.001$  mm, over-focus = +1.2 nm is added on the most right of the lower row, as arrows indicated. It is clearly seen that this image differs from the corresponding calculated image with complementary parameters on its left. The atomic model is shown on the right of the upper row.

image ( $a+b$ ) can be regarded as a measure for the non-linear contribution to the image contrast; as it is zero only in the validity range of the linear imaging theory. In this range (column at 0.5 nm), the difference image ( $a-b$ ) represents the pure phase of the exit wave of  $\text{Si}_3\text{N}_4$ , as amplitude contributions to the image intensity cancel out. For thicker samples the interpretation becomes more complicated.

### 3.1.3. Calculated thickness-focus maps for positive and negative $C_s$

To understand the contrast variations in  $\text{Si}_3\text{N}_4$  for practical relevant values, we have calculated focus-thickness maps along  $[0001]$  direction for positive (Fig. 4a) and negative (Fig. 4b)  $C_s$ , respectively. The coefficient  $C_s$  is set to  $\pm 10 \mu\text{m}$ , the defocus range varies about the Scherzer focus from  $-6.0$  nm (as a convention definition, ‘–’ sign denotes under-focus, ‘+’ sign denotes over-focus) to  $+6.0$  nm and the thicknesses are 2.0, 5.0 and 7.0 nm, respectively. In order to compare contrast differences more easily, the images with complementary parameters (positive  $C_s$ /under-focus and negative  $C_s$ /over-focus) are presented from left to the right. As discussed above (Fig. 3) for the case of Scherzer focus, the images with complementary parameters (Fig. 4a and b) are not complementary to each other even at a thickness as thin as 2 nm. Differences increase with specimen thickness. For example, the images to the left side of about Scherzer focus conditions (defocus = 0) in the thickness row “2.0 nm” in Fig. 4a (positive  $C_s$ ) and 4b (negative  $C_s$ ) show, as expected, dark and white atom contrast, respectively. However, the corresponding images in the “7.0 nm” rows exhibit white atom contrast for both positive and negative  $C_s$ . When comparing the sharpness of the corresponding white dumbbell images (compare e.g., the images in Fig. 4a, 7 nm row, defocus values from  $-4$  to  $-1$  nm with those in Fig. 4b, 7 nm row, defocus values from 1 to 4 nm), we see already by naked-eye inspection that, in contrast to the

case for thinner samples, positive  $C_s$  and under-focus conditions may result in sharper white atom column images.

## 3.2. Experimental observations on $\beta$ - $\text{Si}_3\text{N}_4$

### 3.2.1. Experiments at negative and positive $C_s$

Fig. 5 presents a series of experimental HRTEM images (superimposed with the atomic model) taken at negative spherical aberration ( $C_s \sim -0.5 \mu\text{m}$ ) and different defoci (over-focus: 13 nm (a) and 3 nm (b), and under-focus: 1 nm (c) and 5 nm (d)). By comparing experimental images with calculated ones (two clippings of calculated images in Fig. 5f,g are overlaid) we conclude that the thickness is about 4 nm. In agreement with the calculated images, small over-focus (NCSI conditions, white atom columns) and small under-focus (dark atom columns) conditions (Fig. 5b and c) resolve the Si–N dumbbells, but they are sharper under NCSI conditions. By closely examining the structural images, we find minor contrast inside the six-membered ring. It is conjecturable that this contrast arises from the low frequency transfer gap of  $C_s$ -corrected instruments [28]. For larger focus values (under and over-focus), regular flower-like patterns appear with more complicated contrast as shown in (Fig. 5a and d). In these cases single atom column and dumbbells are not resolved.

Fig. 5e shows the calculated phase contrast transfer functions, ( $\lambda = 1.97$  pm and  $C_s = -0.5 \mu\text{m}$ ), which facilitate the interpretations of the contrast reversals in Fig. 5a–d, as it is clearly seen that the CTF reversals accordingly from over-focus to under-focus. Since a small under-focus (Fig. 5c) does not significantly reduce the resolution (which is still close to information limit) and changes only slightly the delocalization, the Si–N dumbbells are still imaged at almost the same resolution as in Fig. 5b. (Compare red dotted curve and black dashed-dotted curve, which give



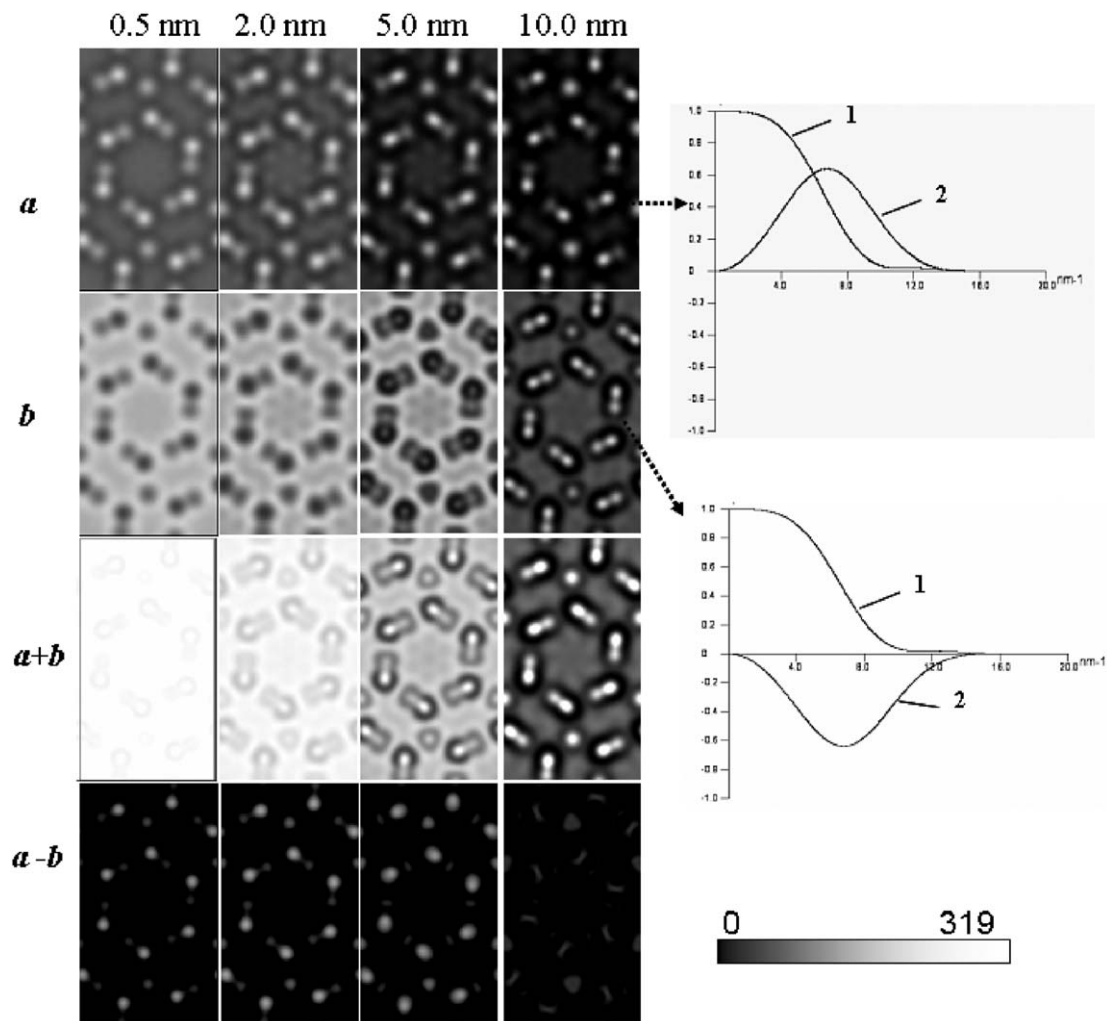


**Fig. 3.** Calculated HRTEM  $\beta$ - $\text{Si}_3\text{N}_4$  [0001] images under complementary parameters ( $\pm C_s$  and  $\mp \Delta f$ ) for thicknesses  $t = 0.5, 2.0, 5.0$  and  $10.0$  nm, respectively. The first row, image series (a), is calculated under the condition of negative  $C_s$  ( $-0.01$  mm) and over-focus ( $+4.3$  nm), the second row, image series (b), is calculated under positive  $C_s$  ( $+0.01$  mm) and under-focus ( $-4.3$  nm). The sum image ( $a+b$ ) and difference image ( $a-b$ ) for different thickness are presented in the rows below. The corresponding amplitude (1) and phase (2) contrast transfer functions (CTF) for the case (a) and (b) are shown on the right. Parameters for the CTF calculations are: semi-convergence angle =  $0.2$  mrad and acceleration voltage =  $300$  kV. The greyscale is shown in the range of  $0$ – $319$ .

nearly the same first zero crossovers). With an increase of under-focus (see Fig. 5d, corresponding to magenta short-dashed CTF in Fig. 5e), image delocalization is dominant in the image. The first zero crossover of the CTF (magenta short-dashed curve in Fig. 5e) is located at  $10\text{ nm}^{-1}$ . As its reciprocal value is larger than the spacing  $0.094\text{ nm}$  of Si–N dumbbell (see the labelled line), it is thus impossible to resolve the Si–N dumbbell and discern the isolated N atom columns.

Overlapped with the atomic model, the HRTEM images (see also the larger view in Fig. 5f and g) reveal that the orientation of the  $\text{Si}_3\text{N}_4$  grain is along  $[000\bar{1}]$  direction (compared to Fig. 1). Fig. 6a shows white atom contrast too, but was obtained under around  $+1\text{ }\mu\text{m}$  positive  $C_s$  value and over-focus of  $3.0\text{ nm}$ . Under such conditions, the contrast delocalization can be very small [15], however, the Si–N dumbbells seem not as clearly separated as in the case of NCSI imaging condition (Fig. 5b). Contrast differences in Si–N dumbbells and in the individual N atom columns are noticeable (see the discussion in Section 3.2.2). The Si–N dumbbells in Fig. 6a are clockwise oriented in contrast to their anticlockwise orientation in Fig. 5b. The FFT (Fig. 6b) shows that the

corresponding Fourier components of the structural image extend into the sub-Ångström region. A reflection corresponding to the  $0.094\text{ nm}$  Si–N dumbbell spacing is indicated. Higher frequencies might be originated from double diffraction.

So far white atom contrast was obtained using over-focus condition, both for negative and positive  $C_s$  values. However, as seen above in Fig. 3 (image b,  $10\text{ nm}$  column) and 4a ( $7\text{ nm}$  row), white atom contrast will arise for thicker samples also with positive  $C_s$  at under-focus conditions. This behaviour has been experimentally confirmed. Fig. 7 shows an image obtained under positive  $C_s$  and under-focus conditions at a thicker specimen area of  $\sim 7\text{ nm}$ . Single N atom columns are clearly seen although Si–N dumbbells are hardly resolved (see the discussion in Section 3.2.2). In agreement with the calculated thickness/defocus map (Fig. 4a,  $7\text{ nm}$  row, under-focus conditions), the atom columns are not imaged black but white. This effect can be attributed to increased contribution of amplitude contrast. A detailed comparison of experimental images for thicker sample areas obtained under different imaging conditions will be the target of future work. However, in practice it might be often difficult to

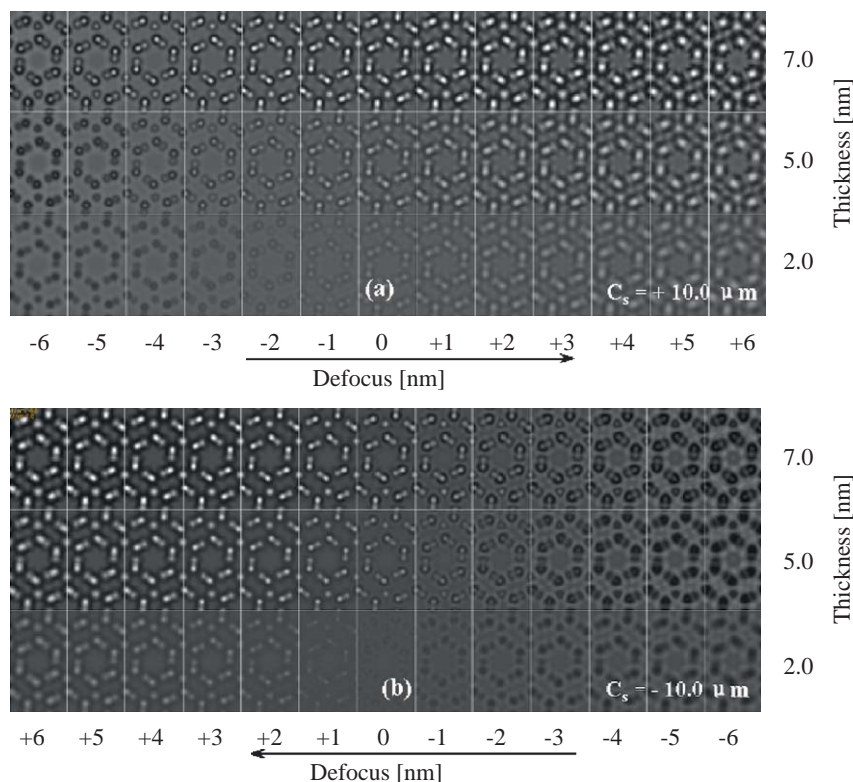


**Fig. 4.** Calculated defocus-thickness maps of HRTEM images of  $\beta$ - $\text{Si}_3\text{N}_4$   $[000 \bar{1}]$  obtained for different spherical aberration ( $C_s$ ), (a)  $C_s = +10 \mu\text{m}$  and (b)  $C_s = -10 \mu\text{m}$ . The defocus ranges from  $-6.0 \text{ nm}$  (under-focus) to  $+6.0 \text{ nm}$  (over-focus), the specimen thickness is  $2.0$ ,  $5.0$  and  $7.0 \text{ nm}$ , respectively. For better comparison, image (a) is flipped vertically. Please note that the contrasts in (a) is not fully complementary to image (b).

prepare very thin samples fulfilling linear imaging conditions, therefore the optimum imaging condition (positive or negative  $C_s$ , over- or under-focus) for different sample thicknesses of the particular material should be studied in forehand to the experiments.

### 3.2.2. Factors influencing the resolution of the Si–N dumbbells

In fact, the general difficulty for imaging the Si–N dumbbells is that this spacing is close to the information limit of our microscope. The crystal has to be aligned perfectly however local variation due to specimen bending might introduce small shifts in the image of atom columns. As a consequence, the dumbbell spacing may remain unresolved. With a  $C_s$ -corrected microscope, tiny mistilt of crystal can be tolerated for optimum phase shift achieved in an aberration-corrected electron microscope [29].

Our experimental images (particularly noticeable in Fig. 5f) show that not all dumbbells are resolved with equal accuracy. As our crystal was aligned most perfectly, this effect might be addressed to residual aberrations, which leads to the breaking symmetry of the phase plate if neglecting nonlinear effects in the experiments. Therefore, the entire sets of dumbbells, i.e. Figs. 5f and 6a, inside special planes are clearly resolved while next parallel plane dumbbells are not.

To minimise the aberrations by taking into account the measured values, one could calculate a numerical phase-plate with which the images could be corrected. This is done by, for example, through-focus exit-wave function reconstruction technique (TF-EWR) [28]. To separate the effect of mistilt accurately

from the effect of residual aberrations is the aim of our on-going work.

## 5. Summary

Using the spherical aberration as an additional tuneable parameter for optimizing resolution and contrast, we have obtained images of the  $\beta$ - $\text{Si}_3\text{N}_4$  six-membered ring structure in  $4\text{-nm}$ -thick  $\text{Si}_3\text{N}_4$  by applying negative  $C_s$  imaging (NCSI, negative  $C_s$ , over-focus) conditions, resulting in sharp white atom contrast. In adjacent grains, Si–N dumbbells with a dumbbell spacing of  $0.94 \text{ \AA}$  were imaged along  $[000 \bar{1}]$  and along  $[000 1]$  projections, respectively, giving a direct view on the dumbbell orientations along the  $6_3$ -screw axis. Minor contrast inside the six-membered ring may be addressed to the low frequency transfer gap of  $C_s$ -corrected instruments. In the case of thicker samples ( $7 \text{ nm}$ ) it was shown, in agreement with calculations that white atom contrast of Si–N dumbbells is obtained also at positive  $C_s$  and under-focus. However, the dumbbell image is less sharp as for the case of thinner samples and NCSI imaging conditions. Further experimental work and calculations are addressing the problem of defining imaging parameters for optimum contrast for differently thick  $\text{Si}_3\text{N}_4$  samples.

We showed by extended image calculations for  $\langle 0001 \rangle$   $\text{Si}_3\text{N}_4$ , that image intensities obtained with complementary parameters ( $\pm C_s$  and  $\mp$  defocus) are only complementary to each other for very thin sample thicknesses ( $t < 0.5 \text{ nm}$ ). For such thin samples (in the thickness range of the validity of the linear imaging theory), a simple method was proposed for pure phase contrast imaging.

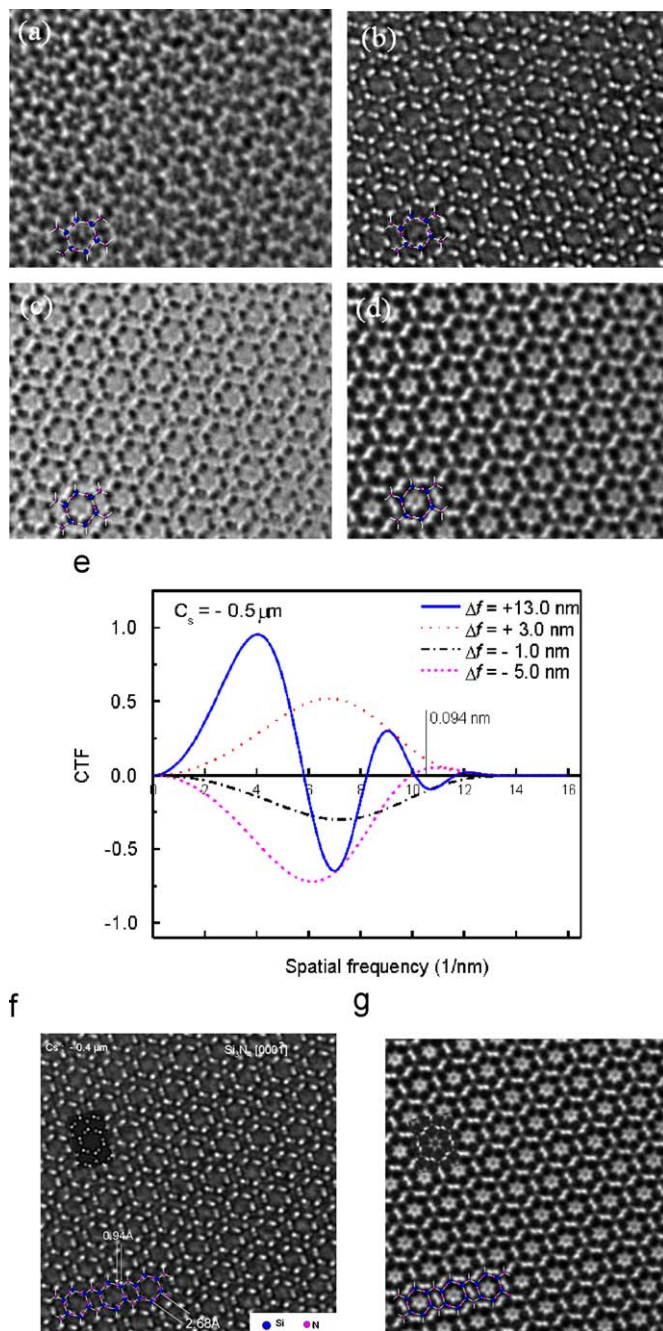


**Fig. 5.** Experimental HRTEM images of  $\beta$ - $\text{Si}_3\text{N}_4$  [0 0 0  $\bar{1}$ ] taken under negative  $C_s$  ( $\sim -0.5 \mu\text{m}$ ) at different defoci; from an over-focus of 13.0 nm (a) and 3.0 nm (b) to an under-focus of 1.0 nm (c) and 5.0 nm (d). The phase contrast transfer function (CTF) (e) showing the phase contrast transfer changes with the corresponding defoci. Parameters for the CTF calculations are: wavelength  $\lambda = 1.97 \text{ nm}$ ,  $C_s = -0.5 \mu\text{m}$ , and semi-angle of beam convergence =  $0.2 \text{ mrad}$  (f) and (g) include the images presented in (a) and (b), respectively, but show a larger area of  $\text{Si}_3\text{N}_4$ , and two clippings of calculated images (thickness =  $4.0 \text{ nm}$ , under-focus  $1 \text{ nm}$  and over-focus  $13 \text{ nm}$ ) are overlaid on the experimental images. Note that the Si and N atom contrasts sensitively vary with defocus changes. An atomic model along [0 0 0  $\bar{1}$ ] is superimposed on the experimental images.

## Acknowledgement

The authors are grateful to Professor Harald Rose for inspiring and stimulating discussions as well as Professor Max Haider for useful discussions related to the accuracy of the aberration coefficients measurements. We thank Dr. Andrey Chuvilin

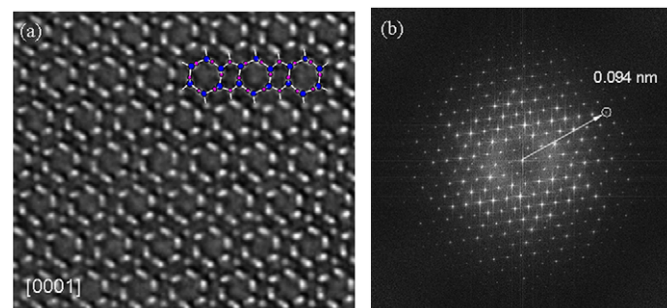


**Fig. 6.** (a) HRTEM image of  $\beta$ - $\text{Si}_3\text{N}_4$  [0001] acquired under a small positive  $C_s$  ( $\sim +1 \mu\text{m}$ ) and under-focus, and a magnification of  $620 \text{ Kx}$  with a sampling rate of  $29 \text{ pm}$  per pixel. Please note that the orientation of the  $6_3$ -screw axis differs from Fig. 5b, (b) FFT of (a), the Si–N dumbbell ( $0.094 \text{ nm}$ ) are clearly transferred by the microscope, but further reflection might result from double diffraction.

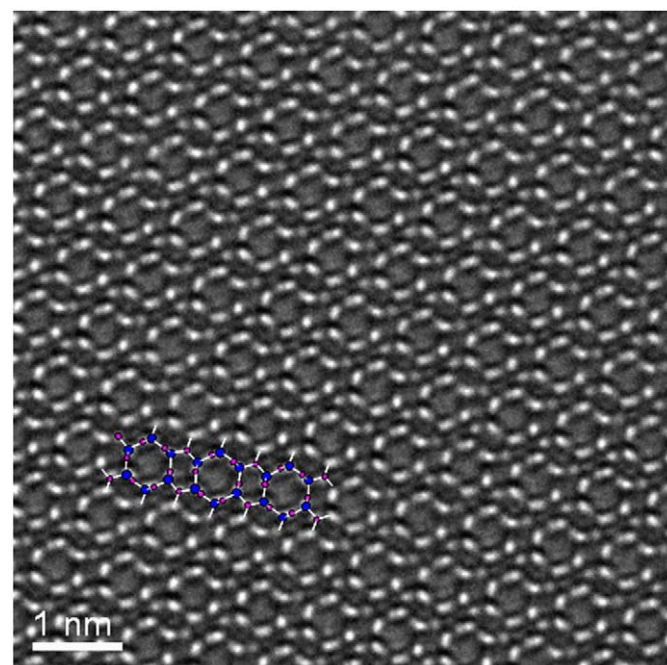


**Fig. 7.** HRTEM image of  $\beta$ - $\text{Si}_3\text{N}_4$  [0 0 0 1] acquired under positive  $C_s$  ( $\sim +10 \mu\text{m}$ ) and under-focus ( $-3 \text{ nm}$ ) for a  $\sim 7\text{-nm}$ -thick sample area (magnification:  $1.25 \text{ Mx}$ , sampling rate:  $14 \text{ pm}$  per pixel). Note that the atom columns are imaged white contrast. An atomic model along [0 0 0 1] is superimposed on the experimental image.

(University Ulm) for helpful discussions with respect to image calculation, and Professor Werner Mader and Dr. Wilfried Assenmacher at University of Bonn for useful hints in precisely determining the spacing of Si–N dumbbells along  $\langle 0001 \rangle$  projection.

## References

- [1] K. Hiraga, K. Tsuno, D. Shindo, M. Hirabayashi, S. Hayashi, T. Hirai, *Philos. Mag.* A47 (1983) 483.
- [2] M. Rühle, *Adv. Mater.* 9 (1997) 195.
- [3] G.B. Winkelman, C. Dwyer, T.S. Hudson, D. Nguyen-Manh, M. Döblinger, R.L. Satet, M.J. Hoffmann, D.J.H. Cockayne, *Philos. Mag. Lett.* 84 (2004) 755.
- [4] A. Ziegler, J.C. Idrobo, M.K. Cinibulk, C. Kisielowski, N.D. Browning, R.O. Ritchie, *Science* 306 (2004) 1768.

- [5] N. Shibata, S.J. Pennycook, T.R. Gosnell, G.S. Painter, W.A. Shelton, P.F. Becher, *Nature* 428 (2004) 730.
- [6] A. Thust, W.M.J. Coene, M. Op de Beeck, D. Van Dyck, *Ultramicroscopy* 64 (1996) 211.
- [7] C. Kisielowski, C.J.D. Hetherington, Y.C. Wang, R. Kilaas, M.A. O'Keefe, A. Thust, *Ultramicroscopy* 89 (2001) 243.
- [8] M.A. O'Keefe, L.F. Allard, D.A. Blom, J. Electron. Microsc. 54 (2005) 169.
- [9] A. Ziegler, C. Kisielowski, R.O. Ritchie, *Acta Mater.* 50 (2002) 565.
- [10] M. Svete, W. Mader, IMC16, September 3–8, 2006, Sapporo, Japan, 2006, p. 951.
- [11] C.L. Jia, M. Lentzen, K. Urban, *Science* 299 (2003) 870.
- [12] H. Rose, *Optik* 85 (1990) 19.
- [13] S. Uhlemann, M. Haider, *Ultramicroscopy* 72 (1998) 109.
- [14] M. Lentzen, B. Jahn, C.L. Jia, A. Thust, K. Tillmann, K. Urban, *Ultramicroscopy* 92 (2002) 233.
- [15] H. Rose, Private communication, 2008 and Bildentstehung im Elektronenmikroskop, lecturescript (pdf-file) available from: info@CEOS-GmbH.de.
- [16] C.-L. Jia, M. Lentzen, K. Urban, *Microsc. Microanal.* 10 (2004) 174.
- [17] M. Lentzen, *Microsc. Microanal.* 12 (2006) 191.
- [18] M. Lentzen, *Ultramicroscopy* 99 (2004) 211.
- [19] Z.L. Zhang, U. Kaiser, *Microsc. Microanal.* 13 (Suppl. 1) (2007) 892.
- [20] M. Svete, L. Houben, K. Tillmann, W. Mader, *Microsc. Microanal.* 13 (Suppl. 3) (2007) 30.
- [21] M. Svete, W. Mader, EMC 2008 Proceedings, Vol. 1, p. 159.
- [22] <<http://www.uni-ulm.de/elektronenmikroskopie/mattem/>>.
- [23] F. Zemlin, K. Weiss, P. Schiske, W. Kunath, K.-H. Herrmann, *Ultramicroscopy* 3 (1978) 49.
- [24] P.A. Stadelmann, *Ultramicroscopy* 21 (1987) 131.
- [25] D. du Bouay, N. Ishizawa, T. Atake, V. Streltsov, K. Furuya, F. Munakata, *Acta Crystallogr. B* 60 (2004) 388.
- [26] J.H. Chen, H.W. Zandbergen, D. Van Dyck, *Ultramicroscopy* 98 (2004) 81.
- [27] K. Urban, in: *Proceeding of the Microscopy Conference*, August 28–September 2, 2005, Davos, Switzerland, p. 399.
- [28] K. Tillmann, A. Thust, K. Urban, *Microsc. Microanal.* 10 (2004) 185.
- [29] B. Kabius, M. Haider, S. Uhlemann, E. Schwan, K. Urban, H. Rose, J. Elec. Microsc. 51 (2002) S51.